Journal of
Mechanics of Materials and Structures

MEASURING IMPACT RESPONSES OF FOAMED POLYMERS

James F. Wilson

Volume 1, Nº 4 *April 2006*

mathematical sciences publishers

JOURNAL OF MECHANICS OF MATERIALS AND STRUCTURES
Vol. 1, No. 4, 2006

MEASURING IMPACT RESPONSES OF FOAMED POLYMERS

JAMES F. WILSON

A unique dual pendulum system was developed to measure single-impact compression responses of foamed polymers. The data, complemented with a mathematical model of impact, led to measures of the material's energy absorption, compression modulus, and damping. Results are presented for a class of open-celled foamed polymers specifically developed for shock mitigation. The experiments employed such materials of four different densities, with impact times ranging in the 1 to 5 ms range and mean impact stresses up to 160 $\mathrm{kN/m^2}$. The results for these materials showed: (1) energy losses of up to 50% of incident energy, with a peak energy absorption per unit volume of 18 $\mathrm{kJ/m^3}$; (2) peak compression modulus of 880 $\mathrm{kN/m^2}$ with strain rates approaching 200 $\mathrm{s^{-1}}$; (3) a mean damping factor of 0.258 with a standard deviation of 0.029. Such data are of practical importance in many shock-mitigating applications, including prostheses, floor pads and cushions, gloves for hand-held vibrating tools, grips for hockey sticks and tennis rackets, and soles for sports shoes.

Introduction

This design effort and experimental study was motivated by the need for a relatively simple and accurate experimental system to quantify single-impact responses of foamed polymers. Related studies involving repeated specimen loading have employed costly universal testing machines with sensor-controlled stress or strain, and magnetic shakers for forced harmonic motion of the specimen. Studies based on the these methods are presented in the treatise of Gibson and Ashby [2001], who reviewed the open literature up to 1999 on the properties and mathematical modeling of cellular solids, for both man-made foams and naturally occurring materials such as wood and cancerous bone. Measuring techniques and typical data for complex moduli, based on the forced oscillation method, were reviewed by Deverge and Jaouen [2004]. These sources and their extensive bibliographies did not reveal any experimental systems or impact analyses similar to those discussed here. No damping data were found in the open literature for one-time impact on foamed polymers.

Keywords: foamed polymers, impact response.

Specimen type	Specimen geometry		Static modulus	Mass density
	diameter, mm	thickness, mm	E, kN/m^2	kg/m^3
white	38.1	7.00	143.	370.
blue	38.1	6.40	373.	451.
red	38.1	5.30	336.	421.
black	38.1	4.86	377.	481.

Table 1. Geometric and physical properties of the foamed polymer specimens.

The characteristics that typify the foamed polymer studied herein are: linearly elastic behavior for static strains up to about 30%; an after-impact recovery time of about 30 s or less to the state of nearly zero strain (the initial state); and an open-celled microstructure in which there are small holes in the cell walls. This class of foamed polymer was developed in the late 1980s by an orthopedist and a New England material science laboratory. These materials are commercially available through Implus Footcare, Morrisville, NC. The material is particularly characterized by its capacity to absorb high levels of impact energy, and is thus used as padding for artificial limbs and for the insoles of sports shoes. Four different densities of these materials, designated by color, were evaluated in the present study. Some of their physical properties are listed in Table 1, together with the size of the impact specimens used.

Shown in Figure 1 are scanning electron micrographs of the most dense material (black), magnified 16 and 160 times. This foamed polymer has an average cell diameter of about 0.2 mm. The general shape of these cells closely matches those observed in the micrographs of a polyurethane foam for which the average cell diameter was also about 0.2 mm; see [Gibson and Ashby 2001, p. 178, Figure 5.2(g)]. This comparison suggests that the base material was a form of polyurethane. The properties of the base material such as density and chemical composition cannot be disclosed since they are patented and proprietary.

This presentation begins with a description of a unique dual-pendulum measuring system, which is followed by a mathematical model of impact that identifies the key parameters to be measured. The study concludes with extensive experimental results for the foamed polymers of Table 1: determinations of material impact energy loss, and the effects of impact stress level and strain rate on both material stiffness and impact-induced damping.

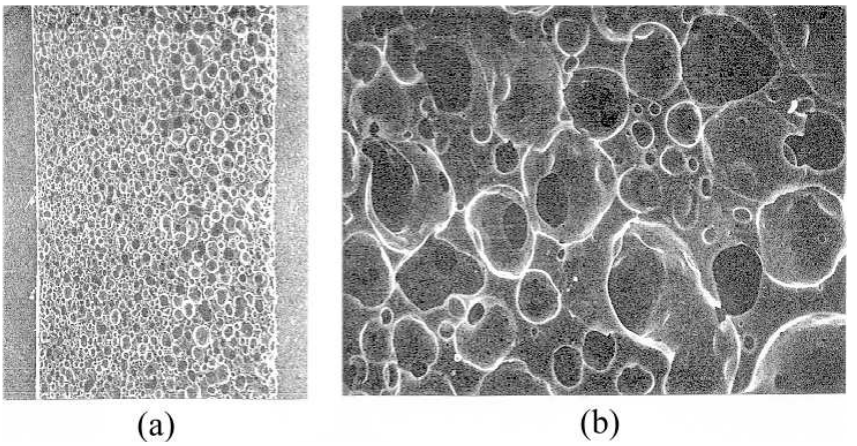

Figure 1. Scanning electron micrographs of the highest density (black) foamed polymer: (a) transverse section through a 4.85 mm thick mat, at 16×; (b) center of mat (a) at 160×. (Courtesy of George W. Pearsall, Duke University.)

Experimental system design

Shown in Figure 2 is the dual pendulum impact system: the driver pendulum and target pendulum, with the foamed polymer specimen of diameter D_0 and thickness h sandwiched between the two impacting die faces. The two pendula are identical. Each consists of a solid steel cylinder of the specimen diameter D_0, with a miniature accelerometer mounted coaxially. The total mass of the steel cylinder and the accelerometer is m, and this assembly is hereafter referred to as a pendulum die. Each steel pendulum arm of length ℓ is rigid or nearly so, and is affixed to the mass center of each die. This arm, together with its bearing shaft, has a mass which is less than one percent of m. The centers of the two arm pivot points are spaced so that the die separation distance is h, the thickness of the test specimen, when the pendula are hanging vertically and at rest. Each pendulum pivot point is the center for a protractor. With a pointer extension to each pendulum arm, the arm angle for a pendulum at rest can be read on its protractor to an accuracy of $\pm 0.1°$.

Shown in Figure 3 are the key positions of the pendula at which the arm angles are measured. The first positions represent the initial static states, in which the driver pendulum arm is hand-held at the visual protractor setting θ_0, and the target pendulum hangs vertically. The second positions are the maximum post-impact rebound angles θ_1 and θ_2 for the driver and target pendulum arms, respectively. These latter extreme rotations are measured either visually or electronically. In the

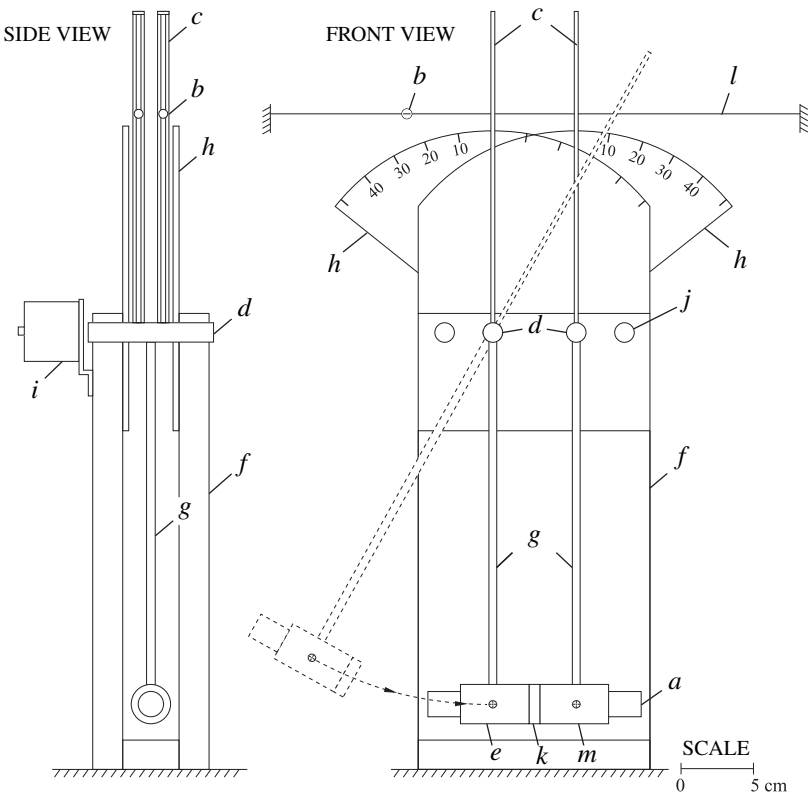

Figure 2. Mechanical design of the dual pendulum system. The components are: a – accelerometer; b – bead; c –steel slotted bead arm; d – steel bearing shaft; e – steel driver die; f – transparent plastic side pannel; g – steel pendulum arm; h – transparent plastic protractor; i – RVDT; j – steel spacer; k – foamed polymer specimen; l – string; m – steel target die.

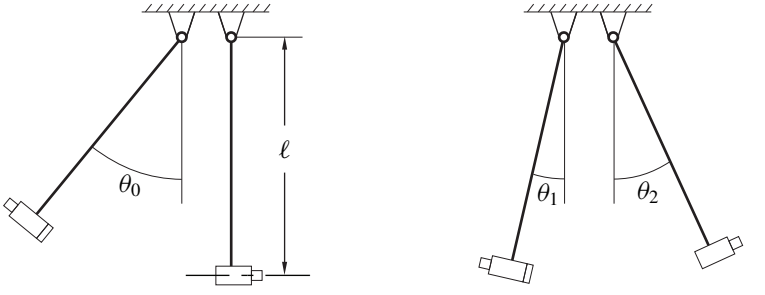

Figure 3. Initial pendulum configuration (left), and maximum rebound configuration (right).

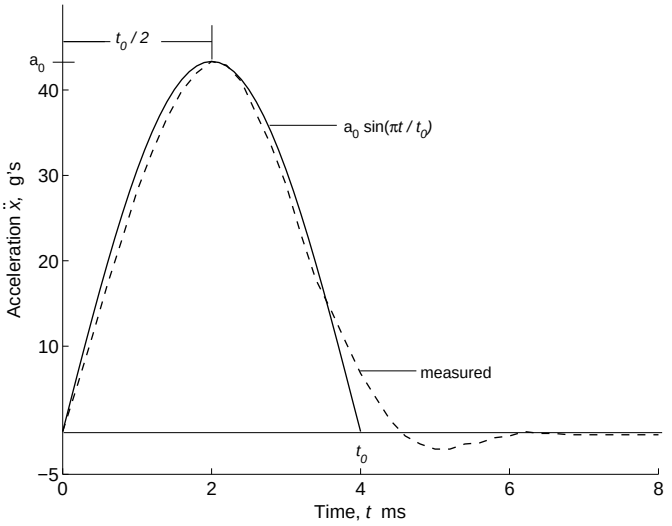

Figure 4. A typical measured acceleration-time history for the impacting driver pendulum, and its best-fit to a half sine curve.

visual method, an extension of the slotted pendulum arm, as shown in Figure 2, pushes a tiny bead along a taut horizontal string, one for each pendulum. There is just enough friction between each relatively weightless bead and string so that the bead does not overshoot its mark corresponding to the maximum arm angle θ_1 or θ_2. Later, when the pendula come to rest, these angles are read on the protractor by aligning the pointer extension with its bead. This visual method for measuring rebound angles gave results that were as accurate and reproducible as the electronic method that used two Schaevitz rotary variable differential transformers (RVDTs) attached to the rotating shafts, as shown in Figure 2. Each RVDT required a 5 volt AC power supply. The voltage output was proportional to rotation, with a sensitivity of 0.01V/degree. At impact, this voltage triggered a digitizing storage oscilloscope, which recorded the time history of rotation for each RVDT.

For each experiment, the driver pendulum was released at a predetermined angle θ_0, its accelerometer output voltage triggered a Hewlett Packard 100 MHz digitizing storage oscilloscope at the instant of impact, and the tangential acceleration-time history $\ddot{x}_1$ of the driver die was recorded and stored for later data processing. The accelerometer was the 25 gram quartz model 353B33 with a 25 volt DC power supply, both manufactured by PCB Piezoelectronics. The sensitivity of this accelerometer was 100 mV/g where $g = 9.81\,\text{m/s}^2$. After numerous preliminary impact experiments using these foamed polymers, it was concluded that a half sine curve of amplitude a_0 and impact time t_0 was a good fit to all measurements $\ddot{x}_1$.

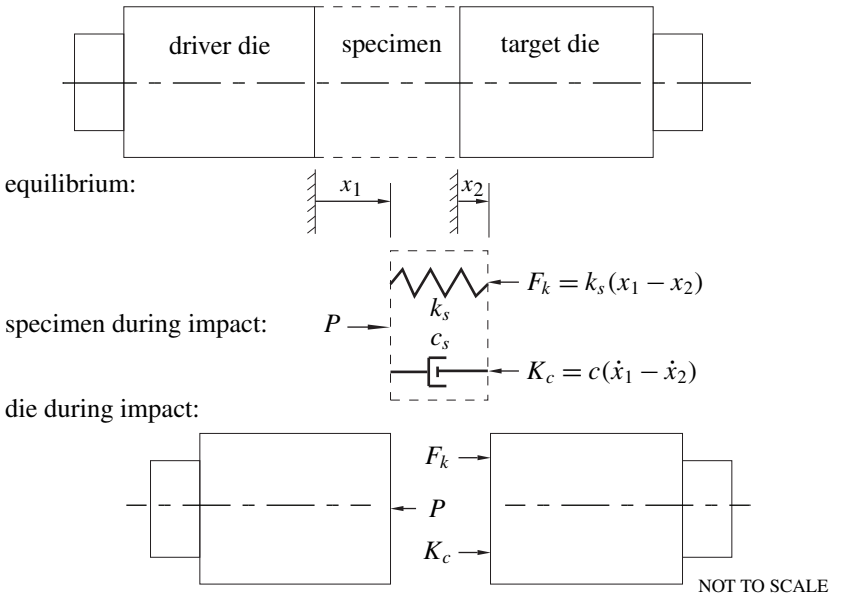

Figure 5. Mathematical models of the two pendulums and the specimen.

That is,

$$\ddot{x}_1 = -a_0 \sin \frac{\pi t}{t_0}, \tag{1}$$

in which the negative sign indicates deceleration. Shown in Figure 4 is a typical experimental trace of $\ddot{x}_1$ and its best-fit half sine curve. Here, the exact time of separation between the specimen and the target die just after impact could not be determined experimentally, and was approximated as t_0.

Given θ_0 and the measured quantities θ_1, θ_2, and $\ddot{x}_1$, the material responses to impact can be computed using the following mathematical model.

Mathematical model of impact

Shown in Figure 5 is the mathematical model of the foamed polymer specimen sandwiched between the two dies. The coordinates x_1 and x_2 are defined as the respective driver and target die face displacements from their static (free hanging) states. The specimen is assumed to behave linearly, or nearly so, to have negligible mass compared to m, and to exhibit damping proportional to the specimen velocity. The representation in Figure 5 reflects these assumptions, in which the specimen's impact force is P and its stiffness and damping parameters are k_s and c_s, respectively. In general, k_s and c_s may vary with time and strain-rate, given an impact time history initiated by θ_0. In these terms, the equations of motion for the

driver pendulum, the specimen, and the target pendulum are, respectively,

$$-P = m\ddot{x}_1, \tag{2}$$

$$P - k_s(x_1 - x_2) - c_s(\dot{x}_1 - \dot{x}_2) = 0, \tag{3}$$

$$k_s(x_1 - x_2) + c_s(\dot{x}_1 - \dot{x}_2) = m\ddot{x}_2. \tag{4}$$

When the first two equations are added to eliminate P,

$$k_s(x_1 - x_2) + c_s(\dot{x}_1 - \dot{x}_2) = -m\ddot{x}_1. \tag{5}$$

The result observed by comparing Equations (4) and (5) is that $\ddot{x}_2 = -\ddot{x}_1$, from which it is concluded that measures of both $\ddot{x}_1$ and $\ddot{x}_2$ would be redundant. The driver die acceleration $\ddot{x}_1$ was the acceleration chosen to be measured.

Kinematics of impact. The kinematics of the compressed specimen are deduced by integrating Equation (1) and using the result that $\ddot{x}_2 = -\ddot{x}_1$. The first integration gives the respective driver and target die velocities as

$$\dot{x}_1 = v_0 - \frac{t_0 a_0}{\pi}\left(1 - \cos\frac{\pi t}{t_0}\right), \qquad \dot{x}_1(0) = v_0, \tag{6}$$

$$\dot{x}_2 = \frac{t_0 a_0}{\pi}\left(1 - \cos\frac{\pi t}{t_0}\right), \qquad \dot{x}_2(0) = 0, \tag{7}$$

which satisfy the stated initial conditions of each die at the instant $t = 0$, or just prior to die impact. The second integration gives the die displacements, subject to zero initial conditions, as

$$x_1 = v_0 t - \frac{t_0 a_0}{\pi}\left(t - \frac{t_0}{\pi}\sin\frac{\pi t}{t_0}\right), \qquad x_1(0) = 0, \tag{8}$$

$$x_2 = \frac{t_0 a_0}{\pi}\left(t - \frac{t_0}{\pi}\sin\frac{\pi t}{t_0}\right), \qquad x_2(0) = 0. \tag{9}$$

The preimpact driver die velocity v_0 in Equations (6) and (8) is deduced by equating the change of potential energy between the driver die's state at θ_0 and the state at first impact ($t = 0$), to the change in kinetic energy between these same states, or

$$mg\ell(1 - \cos\theta_0) = \tfrac{1}{2}mv_0^2, \tag{10}$$

which leads to

$$v_0 = \sqrt{2g\ell(1 - \cos\theta_0)}. \tag{11}$$

The two assumptions inherent in Equation (10) are: energy losses due to bearing and air friction between the two states are negligible, and rotational kinetic energy of the die and arm is negligible in comparison to the to the translational energy of the die. The first assumption was verified by performing free swing tests with the driver arm, in which the specimen and target die were absent. These results showed

that for an initial angular position θ_0, the die arm swung to within one percent of its mirror angle $-\theta_0$. The second assumption was validated by a computation, which showed that the rotational kinetic energy was less than one percent of $mv_0^2/2$ for the dual pendulum apparatus shown in Figure 2.

Energy absorption. The incident energy density, or the energy per volume of the specimen that is available for absorption (Figure 3, left), is defined by

$$W_0 = \frac{4mg\ell}{\pi h D_0^2}(1-\cos\theta_0). \tag{12}$$

Not absorbed by the specimen is the maximum potential energy per volume of the specimen after rebound (Figure 3, right), or

$$W_r = \frac{4mg\ell}{\pi h D_0^2}\big((1-\cos\theta_1)+(1-\cos\theta_2)\big). \tag{13}$$

The specimen's unit energy absorption is the difference of the last two expressions: $W_0 - W_r$. Expressed as a percent of the incident energy density, the unit energy absorption for this nearly frictionless system is thus

$$W = \frac{(1-\cos\theta_0)-(1-\cos\theta_1)-(1-\cos\theta_2)}{(1-\cos\theta_0)} \times 100\%. \tag{14}$$

Impact stress, strain, and strain rate. Since the specimen's impact force is P, Equations (1) and (2) can be used to calculate the time-dependent impact stress, or

$$\sigma = \frac{4P}{\pi D_0^2} = \frac{4ma_0}{\pi D_0^2}\sin\frac{\pi t}{t_0}. \tag{15}$$

The mean stress $\bar{\sigma}$ up to the time $t_0/2$ of maximum compression, and the peak stress σ_p at this time are deduced from the previous equation as

$$\bar{\sigma} = \frac{2}{t_0}\int_0^{t_0/2}\sigma\,dt = \frac{8ma_0}{\pi^2 D_0^2} \qquad \text{and} \qquad \sigma_p = \frac{4ma_0}{\pi D_0^2}. \tag{16}$$

The impact strain ε is based on the relative displacement $x_1 - x_2$ between the die faces. Using Equations (8) and (9), this strain is thus

$$\varepsilon = \frac{x_1 - x_2}{h} = \frac{v_0 t}{h} - \frac{2t_0 a_0}{\pi h}\Big(t - \frac{t_0}{\pi}\sin\frac{\pi t}{t_0}\Big), \tag{17}$$

in which v_0 is given by (11). The average strain rate up to maximum compression at $t = t_0/2$, as deduced from Equations (6) and (7), is defined as

$$\dot{\varepsilon}_a = \frac{2}{t_0 h}\int_0^{t_0/2}(\dot{x}_1 - \dot{x}_2)\,dt = \frac{v_0}{h} - \frac{2t_0 a_0}{\pi h}\Big(1-\frac{2}{\pi}\Big). \tag{18}$$

Specimen stiffness-damping constraint. A constraint relationship between k_s and c_s can be computed by time averaging (5), using (1). That is,

$$\frac{1}{t_0}\int_0^{t_0}\big(k_s(x_1-x_2)+c_s(\dot{x}_1-\dot{x}_2)\big)\,dt=\frac{ma_0}{t_0}\int_0^{t_0}\sin\frac{\pi t}{t_0}\,dt. \tag{19}$$

Let k_s and c_s be constant, on the average, and integrate (19) after substituting for the displacements and velocities given by Equations (6)–(9). The result is

$$k_s=\frac{4\pi^2 ma_0-2\pi^2(\pi v_0-2t_0a_0)c_s}{\pi^3 t_0v_0-2\pi^2t_0^2a_0+8t_0^2a_0}, \tag{20}$$

in which v_0 is given by (11).

Impact damping. The nondimensional damping factor ζ, commonly employed in linear dynamic systems, is defined as

$$\zeta=\frac{c_s}{2\sqrt{k_sm}}. \tag{21}$$

Energy methods are now used to predict an explicit equation for ζ. The difference of peak potential energies for the initial and rebound states, depicted in Figure 3, is the energy lost in specimen damping (subject to the assumptions already discussed). This loss is

$$\Delta E=mg\ell(1-\cos\theta_0)-mg\ell(1-\cos\theta_1)-mg\ell(1-\cos\theta_2). \tag{22}$$

A second form for ΔE is based on the damping power, or the product of the damping force $c_s(\dot{x}_1-\dot{x}_2)$ and the relative die velocity $(\dot{x}_1-\dot{x}_2)$. The energy loss is this product integrated over the die-specimen contact time t_0, or

$$\Delta E=c_s\int_0^{t_0}(\dot{x}_1-\dot{x}_2)^2\,dt. \tag{23}$$

When Equations (22) and (23) are equated and the velocities $\dot{x}_1$ and $\dot{x}_2$ of Equations (6) and (7) are substituted, the resulting equation can be solved for ζ. After performing the integrations and regrouping the parameters, this leads to

$$c_s=\frac{\pi^2mg\ell(\cos\theta_1+\cos\theta_2-\cos\theta_0-1)}{\pi^2t_0v_0^2-4\pi t_0^2a_0v_0+6t_0^3a_0^2}. \tag{24}$$

Thus, with c_s and k_s of Equations (24) and (20), the damping factor ζ can be computed from Equation (21).

The results of this impact analysis are summarized as follows. Given the apparatus and specimen parameters (m, ℓ, D_0, h), and imposing the initial angle θ_0, measures of the quantities $(\theta_1, \theta_2, a_0, t_0)$ give measures of the specimen's key responses. These measures are: the percent of the incident energy absorbed, (14);

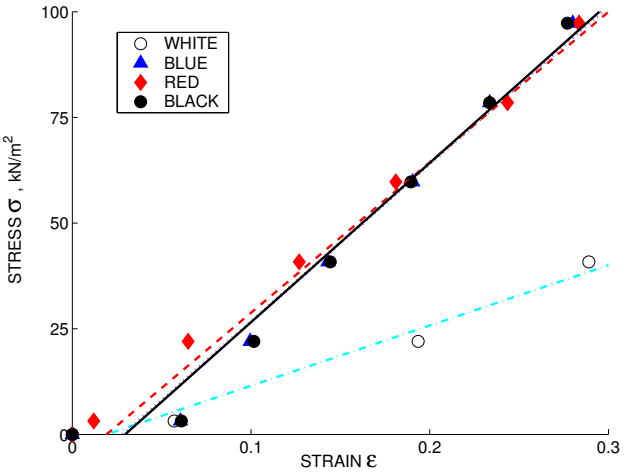

Figure 6. Stress-strain behavior for the four foamed polymers at the low strain rate of about 0.001 s^{-1}.

the stress-strain behavior, Equations (15) and (17); the mean compressive stress and strain rate, Equations (16) and (18); and the stiffness and damping properties, Equations (20), (21), and (24). The experiments to measure $(\theta_1, \theta_2, a_0, t_0)$ are now described.

Experimental protocol and measurements

The foamed polymer specimens described in Table 1 were cut from the as-received sheet material with a sharp steel cookie-cutter die of the same diameter as the impacting die, or 38.1 mm. One set of specimens was used for the standard compression tests, and the other set was used for the impact experiments.

The uniaxial compression tests for each of the four materials were all performed at the rather slow strain rate of about 0.001 s^{-1}. The results are the stress-strain data shown in Figure 6, with a least-squares straight line fit for each material. The slope of each line gives the static modulus E, which is strictly valid only for the stated strain rate. These values of E are listed in Table 1. These results indicate that the four materials behave linearly, or nearly so, up to strains of about 30%, and lend credibility to the hypothesized linear mathematical model.

The protocol for the impact experiments was as follows. The black specimen, defined as the reference specimen, was glued to the die face of the driver pendulum. This pendulum arm was then hand-held at $\theta_0 = 10°$ and released. Then the voltage-time history representing $\ddot{x}_1$ was recorded by the digital storage oscilloscope, which also displayed to four significant figures the peak voltage representing a_0 and the rise time $t_0/2$ to this peak. Using the accelerometer's calibration factor of 100

mV/g, the peak voltage was converted to the peak acceleration a_0, expressed in units of g. Then the first rebound angles θ_1 and θ_2 were measured by one of the two procedures already explained (the bead method was preferred for its simplicity). This same experimental procedure was repeated four more times for $\theta_0 = 10°$. Based on these five trial runs, the arithmetic average (mean value) was computed for each of the four measured quantities $(\theta_1, \theta_2, a_0, t_0)$. This procedure was then repeated for $\theta_0 = 20°$, 30°, and 40° using the same black specimen. A time lapse of at least 60 s was allowed between each impact, so that the specimen could regain its initial thickness.

The sixteen data sets so obtained for the black specimen are listed in Table 2, together with the four incident energy density levels W_0, which were computed from (12) for each respective initial pendulum angle $\theta_0 = 10, 20, 30, 40°$. Here $m = 0.461$ kg (which includes the accelerometer's mass) and $\ell = 0.239$ m. The four incident energy density levels of the black specimens were chosen to be the same as those for the nonblack specimens, as shown in the W_0 column of Table 2. The corresponding values of θ_0 for the nonblack specimens, computed from (12), were all somewhat higher than their black specimen counterparts at $\theta_0 = 10, 20, 30, 40°$,

Specimen type	W_0, kJ/m^3	θ_0, °	Measured mean of five trials θ_1, °	θ_2, °	a_0, g	t_0, ms
white	2.96	12.0	4.42	7.48	7.72	4.62
	11.8	24.1	9.10	17.0	17.0	3.84
	26.1	36.2	15.2	24.8	26.8	3.60
	45.6	48.5	16.8	32.0	35.5	3.44
blue	2.96	11.5	4.44	6.82	14.4	2.43
	11.8	23.0	8.90	15.7	28.5	2.03
	26.1	34.6	12.5	23.8	43.2	1.92
	45.6	46.2	16.7	31.5	56.8	1.87
red	2.96	10.8	4.26	6.52	13.1	2.61
	11.8	20.9	7.26	14.2	25.8	2.19
	26.1	31.4	11.6	22.3	38.6	2.24
	45.6	41.9	14.3	29.6	52.2	2.18
black	2.96	10.0	4.26	6.16	14.8	1.74
	11.8	20.0	7.40	14.1	30.8	1.62
	26.1	30.0	12.5	20.9	47.1	1.41
	45.6	40.0	15.4	27.8	62.5	1.44

Table 2. Dual-pendulum impact measurements.

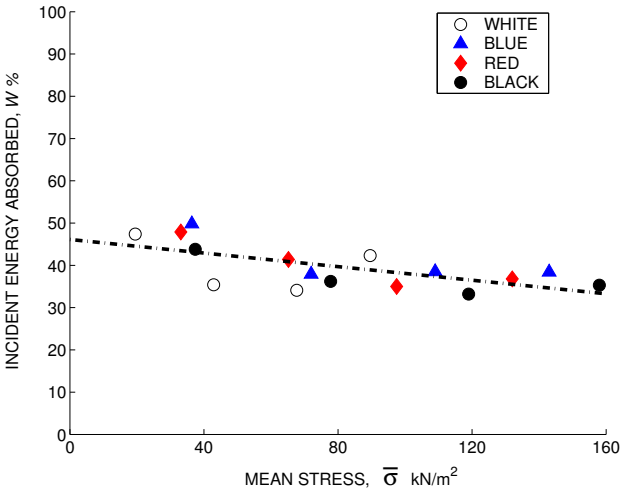

Figure 7. Influence of the mean impact stress on the percent of the incident specimen energy absorbed during impact.

which reflects the differences in specimen thicknesses. The matching of incident energy density levels allows for later comparisons of dynamic responses among specimens of unequal volume.

Using the same experimental protocol as for the black specimen, but with the stated θ_0 values, the sixteen sets of experimental measures $(\theta_1, \theta_2, a_0, t_0)$ for each white, blue, and red specimen were obtained. Again, each numerical entry of each set represents a five-trial average. Such results were reproducible; that is, given θ_0, the deviation of any one measurement of a five-trial run was within 2% of its corresponding mean value.

Computed responses and discussion

Based on the 16 data sets of Table 2, and the two pendulum parameters $m = 0.461\,\text{kg}$ and $\ell = 0.239\,\text{m}$, the material impact responses predicted by the mathematical model were computed. Computational algorithms and graphic displays were developed using Mathematica [Wolfram 1999]. The results are presented in Figures 7–11. In all of these figures, each data point corresponds to a data set $(\theta_0, \theta_1, \theta_2, a_0, t_0)$, or a row in Table 2.

Shown in Figures 7 and 8 are two measures of energy absorption, each as a function of the mean impact stress $\bar{\sigma}$, defined by Equation (16). The dashed straight line in each figure is the least-squares fit to all data. The percent of the incident energy absorbed, based on Equation (14), is shown in Figure 7, which indicates a weakly decreasing energy loss with increasing $\bar{\sigma}$. The best-fit straight line to these

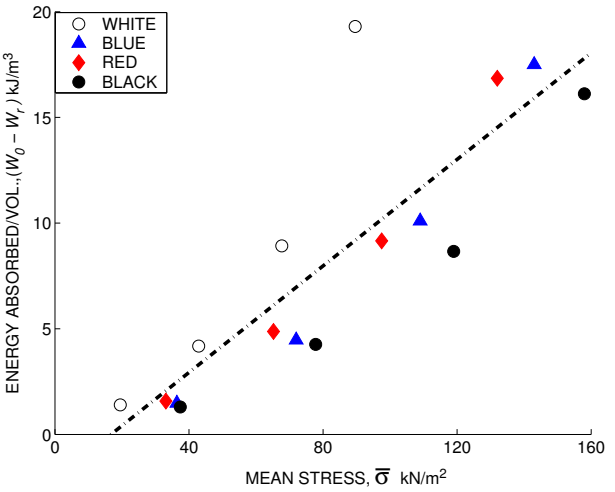

Figure 8. Influence of the mean impact stress on the energy absorbed per unit specimen volume during impact.

data is

$$W(\%) = 46.17 - 0.0803\bar{\sigma}, \tag{25}$$

in which the units of $\bar{\sigma}$ are kN/m^2.

The energy absorbed per unit volume of each specimen, or $W_0 - W_r$ in Equations Equation (12) and Equation (13), is shown in Figure 8. The increase in the unit energy loss W_v is approximately linear with $\bar{\sigma}$, for which the best-fit straight line is

$$W_0 - W_r = 0.126\bar{\sigma} - 2.11, \tag{26}$$

where the units of energy and mean stress are kJ/m^3 and kN/m^2. The data of Figure 8 show that at a given mean stress level $\bar{\sigma}$, the most dense (black) foamed polymer has a consistently lower unit energy loss than the least dense (white) material.

Shown in Figure 9 are the stress-strain curves for all of the specimens, in which each exhibits hysteresis behavior typical of energy-absorbing material. Each curve for each of the four materials has a label a, b, c, or d, which corresponds respectively to the incident unit energy level listed in Table 2, or 2.96, 11.8, 26.1, and 45.6 kJ/m^3. These curves were generated using (15) and (17), which are parametric equations in time t. To each closed curve there corresponds an average strain rate $\dot{\varepsilon}_a$, computed from Equations (18) and (11) for each θ_0. The peak of each closed curve, at $t = t_0/2$, marks the end of increasing compression stress. At the end of impact, assumed to occur at $t = t_0$, the stress is zero. Then each unloaded specimen was observed to recover (along the abscissa to the origin) to nearly its original thickness h in about 30 s. The area enclosed by each of the 16 hysteresis

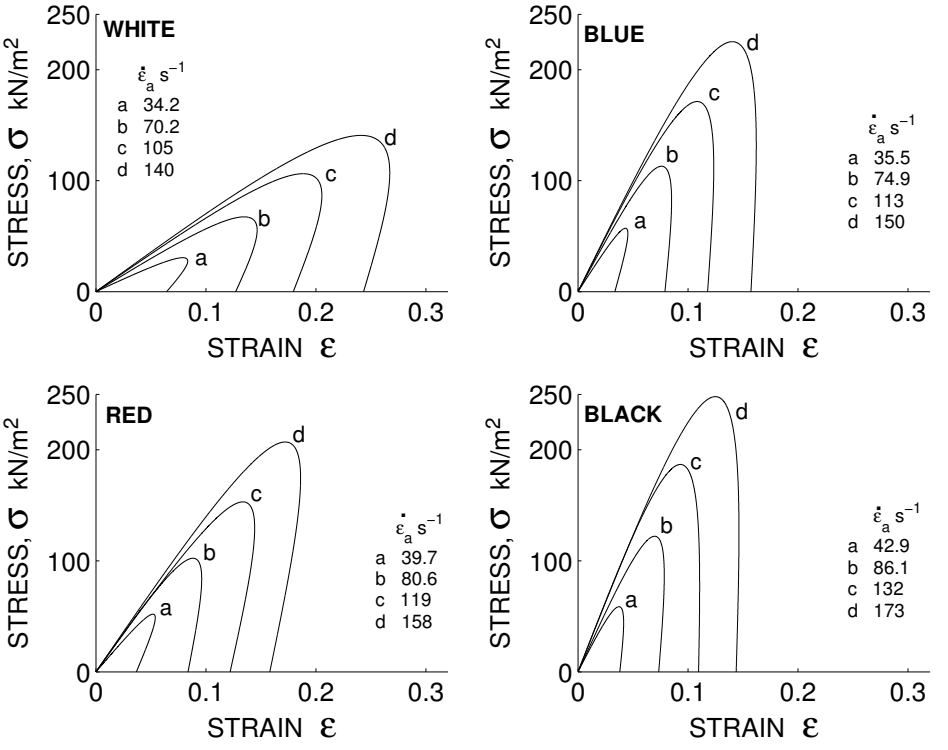

Figure 9. Stress-strain and hysteresis behavior for the foamed polymers, showing the influence of strain rate.

curves in Figure 9 corresponds to the energy absorbed per unit volume, the values of which were also computed using Equation (14) and displayed in Figure 8.

Shown in Figure 10 is a weak dependency of the compression modulus E_c on the average strain rate $\dot{\varepsilon}_a$, for all four materials. This modulus is defined in terms of the elastic stiffness k_s, or

$$E_c = \frac{4hk_s}{\pi D_0^2}. \tag{27}$$

For each material, it appears that E_c approaches a limiting or asymptotic value as $\dot{\varepsilon}_a$ increases. For the highest-density material (black), for instance, $E_c \to 900\,\text{kN/m}^2$ as $\dot{\varepsilon}_a \to 150\,\text{s}^{-1}$. For the two intermediate density materials, the average asymptotic values are nearly the same, or about $700\,\text{kN/m}^2$; and for the least dense material, $E_c \to 300\,\text{kN/m}^2$.

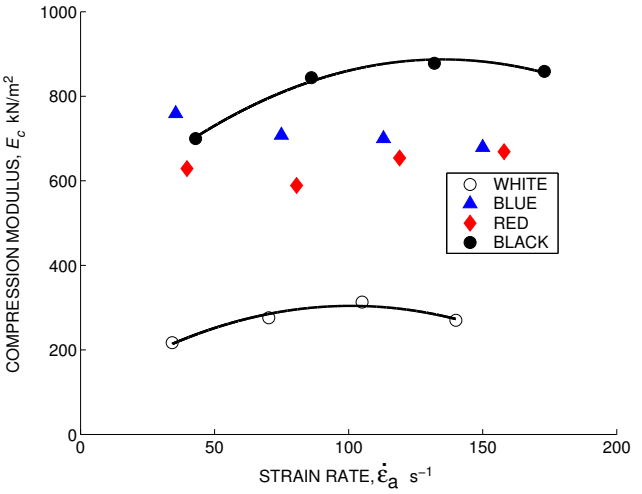

Figure 10. Influence of strain rate on the compression modulus for the four foamed polymers.

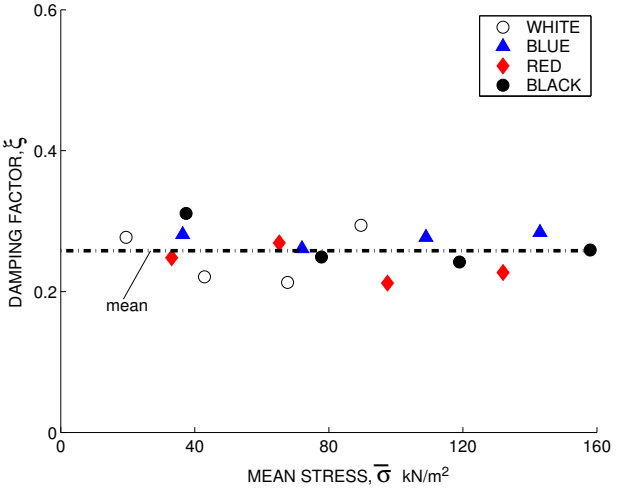

Figure 11. Influence of the mean impact stress on the damping factors for the four foamed polymers.

Shown in Figure 11 is the damping factor ζ, with its weak dependency on the mean level of impact stress $\bar{\sigma}$. The straight line is the least-squares fit (mean value) of data for all four materials, or

$$\zeta = 0.258, \qquad SD = 0.029. \tag{28}$$

Conclusions

This dual-pendulum measuring system is simple in construction and versatile in operation. System bearing-friction was minimized by precision machining and graphite lubrication. The impact energy permanently lost to the apparatus was minimized in two ways: (1) by choosing equal specimen and die diameters, which confined the transmitted acoustic waves to the same diameter cylinders, eliminating most of the energy dispersion in the uniform dies; (2) by assigning more than 99% of a pendulum's mass to the die so that the pendulum's center of percussion was nearly coincident with the die's longitudinal axis of symmetry, thus reducing the horizontal bearing impact reaction force, and its contribution to friction energy loss to nearly zero. Further, by matching each of the four incident energy density levels (a, b, c, d) for the consecutive testing of each specimen type, comparisons of the dynamic responses among specimens of different thicknesses could be made.

That the mathematical model for impact is consistent with the measurements was demonstrated in the following ways:

- For all 16 data sets of Table 2, the following two independent measures for the velocity of the target die just after impact agreed to within about 10%. That is,

$$\dot{x}_1(t{=}t_0) \simeq \sqrt{2gl(1-\cos\theta_1)}. \tag{29}$$

  Here, the left side is the value predicted by Equation (6), and the right side is based on the conservation of energy and the independent measure θ_1.

- The closed area of each of the 16 hysteresis curves of Figure 9 generally agreed within 10% to its counterpart unit energy calculated from Equation (14).

- Consider Figure 9 for a given material. The slope of each stress-strain curve up to about $t = 0.4t_0$ is consistently higher than the slope E of Figure 6 for the same material. Theory predicts that this slope will increase with increasing strain rate, an effect that is due to the accompanying increase in the elastic and damping reaction forces.

Future developments include new and complementary theories of impact for a variety of nonlinear, open or closed-cell materials for which this dual pendulum system can be employed to measure material properties.

Acknowledgements

The author thanks Rhett T. George for his advice on electronic measurements; and the reviewers for their valuable insights.

References

[Deverge and Jaouen 2004] M. Deverge and L. Jaouen, "A review of experimental methods for the elastic and damping characteristics of acoustical porous materials", in *Internoise 2004: The 33rd International Congress and Exposition on Noise Control Engineering*, Prague, Czech Republic, August 22–25 2004, Available at http://www.univ-lemans.fr/~s012782/Deverge_Jaouen_v5.pdf.

[Gibson and Ashby 2001] L. J. Gibson and M. F. Ashby, *Cellular solids: structure and properties*, 2nd ed., Cambridge University Press, Cambridge, 2001.

[Wolfram 1999] S. Wolfram, *The Mathematica book*, 5th ed., Wolfram Media, Champaign, IL, 1999.

Received 11 Dec 2005.

JAMES F. WILSON: jwilson@duke.edu
Pratt School of Engineering, Duke University, 6319 Mimosa Drive, Chapel Hill, NC 27514, United States